SMART: dissipative absorbing layer technique for general elastodynamics equations. Application as S-waves filter in acoustic TI media.

L. Métivier[1,2,*], R. Brossier[2,*], S. Labbé[1,*], S. Operto[3,*], J. Virieux[2,*]

Abstract

Keywords: Seismic Wave Modeling, Hyperbolic Problems, Absorbing Layers, Perfectly Matched Layers, Transverse Isotropic Anisotropy

1. Introduction

Seismic imaging methods such as Full Waveform Inversion (FWI Virieux and Operto [38], Métivier et al. [30, 28]) or Reverse Time Migration (RTM Baysal et al. [6]) require accurate modeling engines for the propagation of seismic waves in infinite or semi-infinite media. To this end, the use of efficient absorbing boundary conditions is mandatory. Moreover, one should be sure that the modeling engine will provide always an answer at each iteration of the inversion and of the migration. The stability is, therefore, a very important property of absorbing conditions.

In 1994, Bérenger [8] introduced the Perfectly Matched Layers (PML) method as an absorbing layer technique for the propagation of electromagnetic waves. The method consists in surrounding the domain of interest by a thin layer in which the incoming waves are damped. This follows the pioneering approach of Cerjan et al. [12], later named as sponge layer technique. An analysis of the PML method at the continuous level shows that the reflection coefficient at the interface between the domain of interest and the layer is zero for all incidence angles. Although this property is lost as soon as the problem is discretized, the amplitude of the parasite reflections remains small, hence ensuring an excellent absorption when the layer is introduced.

Originally designed for the 2D Maxwell's equations, the method has rapidly been extended to 3D Maxwell's equations (Bérenger [9]), acoustics equations (Qi and Geers [34], Diaz and Joly [14], Bermúdez et al. [10]), linearized Euler equations (Hu [21], Hesthaven [20], Abarbanel et al. [1]) and elastodynamics equations (Hastings et al. [19], Collino and Tsogka [13], Basu and Chopra [5], Komatitsch and Tromp [24], Appelö and Kreiss [4]). Extensions of the PML method to convolution-type PML methods (CPML) have been proposed for elastodynamics to improve the discrete reflection coefficient associated with waves propagating at grazing angles (Komatitsch and Martin [23], Martin et al. [27], Martin and Komatitsch [26]).

Despite these remarkable properties, the PML method has a significant setback when applied to elastodynamics equations. Depending on the numerical schemes which is used, the layer can become amplifying, leading to the propagation of spurious numerical discrete modes exponentially increasing. This phenomenon (often referred to as instability in the literature) has been observed in numerous studies, particularly when unstructured meshes are used together with a Discontinuous Galerkin discretization method (see for instance Meza-Fajardo and Papageorgiou [31], Etienne et al. [16], Tago et al. [36]).

In addition, when anisotropy is introduced in the wave propagation equations, the PML become amplifying, regardless of the discretization method which is employed. This intrinsic instability has been first exhibited by Becache et al. [7]. They demonstrate that when the slowness vector and the group velocity are in opposite directions (negative scalar product), the PML becomes amplifying. Later on, Halpern et al. [18] have performed a WKB analysis of PML which shows that the amplification phenomenon is likely to occur

*corresponding author
Email address: ludovic.metivier@ujf-grenoble.fr (L. Métivier)
URL: http://www-ljk.imag.fr/membres/Ludovic.Metivier/ (L. Métivier)
[1]LJK, CNRS, Université de Grenoble, BP 53, 38041 Grenoble cedex 09, France
[2]ISTerre, Université de Grenoble I, BP 53, 38041 Grenoble Cedex 09 France
[3]Géoazur, Université de Nice Sophia-Antipolis, CNRS, IRD, OCA, Valbonne, France

for general first-order hyperbolic systems. Maxwell's and acoustics equations are particular cases for which this amplification does not occur.

Contrary to the PML, the more rudimentary sponge layer technique designed by Cerjan et al. [12] ensures the dissipation of the energy of the solution for general hyperbolic systems. However, the accuracy of this method is not satisfactory: large amplitude spurious reflections are generated at the interface between the layer and the domain of interest for non-zero incidence angles.

On this basis, we are interested in designing a layer technique with same dissipative property as the sponge layer but with an improved accuracy, while keeping the non-amplifying property essential during iterations for inversion or migration. This leads us to consider the SMART layer strategy, proposed in Halpern et al. [18] as a generalization of the 1D study performed earlier by Israeli and Orszag [22]. This method is based on the decomposition of the wavefield into components propagating in different directions. Depending on the position of the layer, only outgoing components are damped, following a selective damping strategy. This decomposition is performed through the definition of spectral projectors on the eigenspaces associated with the matrices defining the symbol of the first-order hyperbolic operator. In Métivier et al. [29], it is proved that, for symmetrizable first-order hyperbolic systems, the SMART layer strategy is dissipative.

In this study, we show that the general first-order elastodynamics equations satisfy this symmetrizability condition, making the SMART layer method a robustly dissipative absorbing layer technique for these equations. We provide numerical experiments comparing PML, sponge layers, and SMART layers which emphasize the robustness of the SMART layers, as well as their better accuracy compared to sponge layers.

In addition, we show that the selective damping strategy on which is based the SMART layer method can be used as a particular S-wave filter. This feature is interesting in the particular case of acoustic anisotropic simulations. Acoustic anisotropic equations have been derived with the purpose of accounting for anisotropy without paying the price of expensive elastodynamics simulations (Alkhalifah [2, 3]). These equations model the propagation of P-waves only, accounting both for dynamic and kinematic effects of anisotropy. However, in certain types of media, for instance anelliptical Transversely Isotropic (TI) media, the propagation of unwanted S-waves is observed. These S-waves can be generated directly at the source, or by P-S conversion on sharp interfaces. New equations constructed from the manipulation of the dispersion relation have been recently proposed by Xu and Zhou [39] to avoid the propagation of these S-waves, yielding the so-called pure quasi-P waves equations. In this study, we propose an alternative solution, consisting in damping directly S-waves around the source and identified reflectors, following the selective damping strategy associated with the SMART layers method.

The paper is organized as follows. In Section 2, we present the SMART method, and recall the main result about the method concerning its dissipative property. In Section 3, we demonstrate that the elastodynamics equations satisfy the symmetrizability condition for the SMART layer method to be robustly dissipative. In Section 4, we show how the SMART layer strategy can be used as an S-wave filter in the particular case of acoustic anelliptical TI media. In Section 5, we provide numerical results emphasizing these two aspects: robustness of SMART layers and application as S-waves filter. A conclusion and perspectives of future work are given in Section 6.

2. The SMART layer method

2.1. Presentation

We consider the general first-order hyperbolic system

$$\begin{cases} \partial_t u + \displaystyle\sum_{j=1}^{d} A_j(x)\partial_j u + A_0(x)u = f(x,t), \quad (x,t) \in \Omega \times [0,T], \quad d \in \mathbb{N}, \\ u(x,0) = u_0(x), \end{cases} \tag{1}$$

where $d \in \mathbb{N}$, is the dimension and

$$\begin{cases} \Omega \subset \mathbb{R}^d, \\ u(x,t) \in L^2\left(\Omega \times [0,T], \mathbb{R}^p\right), \\ u_0(x) \in L^2\left(\Omega, \mathbb{R}^p\right). \\ f(x,t) \in L^2\left(\Omega \times [0,T], \mathbb{R}^p\right), \\ \forall x \in \mathbb{R}^d, \quad A_j(x) \in \mathbb{M}_p\left(\mathbb{R}\right), \quad j = 0, \ldots, d. \end{cases} \tag{2}$$

The components of the solution propagating in the directions j are related to the eigenvalues of the matrices A_j. The amplitude of the eigenvalues of A_j gives the propagation speed of the components of the solution propagating along the direction j. The sign of the eigenvalues of A_j gives the sense of propagation of these components along the direction j. In the following we denote these eigenvalues by

$$\lambda_{j,s}^{\pm}, \quad s = 1, \dots, N_j^{\pm}, \tag{3}$$

where the subscripts + and − are related to the sign of the eigenvalues and $N_j^{\pm}$ denotes the number of positive (resp. negative) eigenvalues of the matrix A_j.

One particular component of the solution may be extracted by projecting the solution onto the eigenspaces of A_j. For instance, the sth components traveling along the axis j in the positive sens is given by

$$B_{j,s}^{+}(x)u, \tag{4}$$

where $B_{j,s}^{+}$ is the projector onto the eigenspace

$$\ker\left(A_j - \lambda_{j,s}^{+} I_p\right). \tag{5}$$

In equation (5), I_p is the identity matrix in $\mathbb{M}_p(\mathbb{R})$. The definition of the SMART layer relies on this extraction. The method aims at damping only outgoing components of the solution. Assuming the domain of interest $\mathring{\Omega}$ is the multi-dimensional box

$$\mathring{\Omega} = \prod_{j=1}^{d} [a_j, b_j], \tag{6}$$

the computational domain Ω is

$$\Omega = \prod_{j=1}^{d} [a_j - L_j, b_j + L_j], \tag{7}$$

where L_j is the layer thickness in dimension j. We introduce the mono-dimensional damping coefficient $d_j(x_j)$

$$\begin{cases} \forall x_j, \;\; a_j < x_j \leq b_j + L_j, \;\; d_j^{-}(x_j) = 0, & \forall x_j, \;\; a_j - L_j \leq x_j \leq a_j, \;\; d_j^{-}(x_j) > 0, \\ \forall x_j, \;\; a_j - L_j \leq x_j < b_j, \;\; d_j^{+}(x_j) = 0, & \forall x_j, \;\; b_j \leq x_j \leq b_j + L_j, \;\; d_j^{+}(x_j) > 0. \end{cases} \tag{8}$$

These coefficients $d_j(x_j)^{\pm}$ are 0 in the domain of interest and smoothly increase in the layer in the j direction. The SMART layer consists in introducing the zero-order term

$$B(x)u = \sum_{i=1}^{d} \sum_{s=1}^{N_j^{+}} d_j^{+}(x_j) B_{j,s}^{+} u + \sum_{i=1}^{d} \sum_{s=1}^{N_j^{-}} d_j^{-}(x_j) B_{j,s}^{-} u, \tag{9}$$

into the initial system (1). The operator $B(x)$ is the sum of the projectors onto all the eigenspaces of the matrices A_j weighted by the damping coefficients $d_j^{\pm}(x_j)$ so that only outgoing components of the solution are damped. We thus obtain the SMART system

$$\begin{cases} \partial_t u + \displaystyle\sum_{j=1}^{d} A_j(x) \partial_j u + A_0(x) u + B(x) u = f(x,t), \;\; (x,t) \in \Omega \times [0,T], \;\; d \in \mathbb{N}, \\ u(x,0) = u_0(x). \end{cases} \tag{10}$$

2.2. Dissipation property

Theorem 1. *Assume that $\forall x \in \Omega$ there exists $S(x)$ symmetric positive definite such that $\forall j = 1, \dots d$, $S(x)A_j(x)$ is symmetric. $S(x)$ is called a symmetrizer of* (1)*. Then we have the energy estimate*

$$\frac{d}{dt} \|u(.,t)\|_S^2 \leq (\gamma + 1) \|u(.,t)\|_S^2 + \|f(.,t)\|_S^2 - 2 \left(S B u, u\right)_{L^2}, \tag{11}$$

where $\|.\|_S$ denotes the norm induced by the symmetrizer S, $(.,.)_{L^2}$ is the standard L^2 scalar product, and γ is defined by

$$\gamma = \sum_{j=1}^{d} \sup_x |\partial_x (S A_j)| + \sup_x |(S A_0)|. \tag{12}$$

The dissipative property of the SMART layer is ensured by the following inequality

$$(S\,Bu, u)_{L^2} \geq 0 \tag{13}$$

A complete proof of this theorem is given in Métivier et al. [29]. The energy estimates can be obtained following standard energy techniques (Kreiss and Lorenz [25]). Here, we review how the inequality (13) ensuring the dissipation can be proved. This property relies on the following lemma.

Lemma 1. *Let $A \in \mathbb{M}_p(\mathbb{R})$. Let $S \in \mathbb{M}_p(\mathbb{R})$ symmetric positive definite such that SA is symmetric. Then the eigenspaces of A form an orthogonal direct sum for the scalar product induced by S on $\mathbb{R}^p$.*

Proof. Let $(u, v) \in \mathbb{R}^p \times \mathbb{R}^p$ be two eigenvectors of A

$$Au = \lambda u, \quad Av = \mu v, \tag{14}$$

where λ and μ are the eigenvalues associated with u and v respectively. We denote the scalar product in $\mathbb{R}^p$ by $< ., . >$. We have

$$< Su, v >= \frac{1}{\lambda} < SAu, v >= \frac{1}{\lambda} < u, SAv >= \frac{\mu}{\lambda} < u, Sv >= \frac{\mu}{\lambda} < Su, v > . \tag{15}$$

Therefore, either

$$< Su, v >= 0, \tag{16}$$

and the eigenvectors u, v are orthogonal for the scalar product induced by S or

$$< Su, v >\neq 0, \quad \lambda = \mu, \tag{17}$$

which means that u and v belongs to the same eigenspace of A. □

The function $u(x,t) \in L^2(\Omega \times [0,T], \mathbb{R}^p)$ can be decomposed according to the direct sum of the eigenspaces of $A_j(x)$ as

$$\forall (x,t) \in \Omega \times [0,T], \quad u(x,t) = \sum_i \alpha_{j,i}(x,t) a_{j,i}(x). \tag{18}$$

Consider $B^+_{j,1}$, the spectral projector on the eigenspace $\ker\left(A_j - \lambda^+_{j,1} I_p\right)$, where $\lambda^+_{j,1}(x)$ is the first positive eigenvalue of the matrix $A_j(x)$. We have

$$B^+_{j,1}(x)u(x,t) = \alpha_{j,1}(x,t) a_{j,1}(x). \tag{19}$$

Therefore,

$$\begin{aligned} \left(S\,B^+_{j,1}u, u\right)_{L^2} &= \int_\Omega < S(x)B^+_{j,1}(x)u(x,t), u(x,t) > dx \\ &= \int_\Omega < \alpha_{j,1}(x,t) S(x) a_{j,1}(x), \sum_i \alpha_{j,i}(x,t) a_{j,i}(x) > dx \\ &= \int_\Omega \sum_i \alpha_{j,1}(x,t)\alpha_{j,i}(x,t) < S(x)a_{j,1}(x), a_{j,i}(x) > dx. \end{aligned} \tag{20}$$

Using the Lemma 1, we find

$$\left(S\,B^+_{j,1}u, u\right)_{L^2} = \int_\Omega \alpha^2_{j,1}(x,t) < S(x)a_{j,1}(x), a_{j,1}(x) > dx. \tag{21}$$

As $S(x)$ is symmetric definite positive, we have

$$\left(S\,B^+_{j,1}u, u\right)_{L^2} \geq 0. \tag{22}$$

The same demonstration is valid for any spectral projectors $B^+_{j,i}$, $B^-_{j,i}$ on the eigenvalues of A_j. Therefore, as B is a linear combination of these projectors weighted by positive functions $d^\pm_j(x_j)$ we have

$$(S\,Bu, u)_{L^2} \geq 0. \tag{23}$$

3. Symmetrizability of the elastodynamics equations

From the previous theorem, we see that the SMART layer strategy is dissipative for any symmetrizable first-order hyperbolic system. In this section, we show that the general 3D elastodynamics equations satisfy this condition. Under the velocity-stress formulation and the Voigt notations, the elastodynamics equations amount to the first-order hyperbolic system

$$\begin{cases} \partial_t u = \dfrac{1}{\rho}\left(A_x\partial_x\sigma + A_y\partial_y\sigma + A_z\partial_z\sigma\right) \\ \partial_t \sigma = C\left(A_x^T\partial_x\sigma + A_y^T\partial_y\sigma + A_z^T\partial_z\sigma\right), \end{cases} \tag{24}$$

where $u(x,t) \in L^2\left(\Omega\times[0,T],\mathbb{R}^3\right)$ and $\sigma(x,t) \in L^2\left(\Omega\times[0,T],\mathbb{R}^6\right)$ are the velocity displacement vector and the stress vector

$$u(x,t) = \left[u_x, u_y, u_z\right], \tag{25}$$

$$\sigma(x,t) = \left[\sigma_{xx}, \sigma_{yy}, \sigma_{zz}, \sigma_{xz}, \sigma_{yz}, \sigma_{xy}\right]. \tag{26}$$

In addition, the quantity ρ is the density, C is the stiffness tensor reduced as the 6×6 matrix C_{ij}, and the matrices A_x, A_y, A_z are

$$A_x = \begin{pmatrix} 1 & 0 & 0 & 0 & 0 & 0 \\ 0 & 0 & 0 & 0 & 0 & 1 \\ 0 & 0 & 0 & 0 & 1 & 0 \end{pmatrix}, \quad A_y = \begin{pmatrix} 0 & 0 & 0 & 0 & 0 & 1 \\ 0 & 1 & 0 & 0 & 0 & 0 \\ 0 & 0 & 0 & 1 & 0 & 0 \end{pmatrix}, A_z = \begin{pmatrix} 0 & 0 & 0 & 0 & 1 & 0 \\ 0 & 0 & 0 & 1 & 0 & 0 \\ 0 & 0 & 1 & 0 & 0 & 0 \end{pmatrix}. \tag{27}$$

The stiffness tensor C is by definition symmetric and positive definite. Its inverse $M = C^{-1}$, known as the compliance matrix, is thus also symmetric positive definite. A simple manipulation of the system (24) yields

$$\begin{cases} \rho\partial_t u = A_x\partial_x\sigma + A_y\partial_y\sigma + A_z\partial_z\sigma \\ M\partial_t\sigma = A_x^T\partial_x\sigma + A_y^T\partial_y\sigma + A_z^T\partial_z\sigma. \end{cases} \tag{28}$$

We define $w \in L^2\left(\Omega\times[0,T],\mathbb{R}^9\right)$ as

$$w = [u,\sigma]^T. \tag{29}$$

We rewrite (28) as

$$S\,\partial_t w = \widetilde{A}_x\partial_x w + \widetilde{A}_y\partial_y w + \widetilde{A}_z\partial_z w, \tag{30}$$

where

$$S = \begin{pmatrix} \rho I_3 & 0 \\ 0 & M \end{pmatrix}, \quad \widetilde{A}_j = \begin{pmatrix} 0 & A_j \\ A_j^T & 0 \end{pmatrix}, \quad j\in\{x,y,z\}. \tag{31}$$

In (31), I_3 denotes the identity matrix of $M_3(\mathbb{R})$. It is important to note that the matrix S is therefore symmetric positive definite, as it is block diagonal with positive definite blocks. In addition, the matrices $\widetilde{A}_j$ are symmetric. The elastodynamics equations (24) are thus equivalent to the first-order hyperbolic system

$$\partial_t w = S^{-1}\widetilde{A}_x\partial_x w + S^{-1}\widetilde{A}_y\partial_y w + S^{-1}\widetilde{A}_z\partial_z w. \tag{32}$$

An obvious symmetrizer for this system is the operator S.

This simple demonstration, inspired from the work of Burridge [11], enlightens the symmetrizability of the elastodynamics equations, through the definition of the compliance matrix M.

4. Acoustic TI modeling and SMART layers as *S*-waves filter

In this section, we focus on the particular case of 2D acoustic transverse isotropic equations. In seismic imaging methods, such as FWI or RTM, taking into account the subsurface anisotropy reveals to be a crucial issue for improving the quality of the results. This can be performed through the use of anisotropic elastic modeling engines. However, as the computational cost of elastic modeling engines can be two to three orders of magnitude higher than their acoustic counterpart, acoustic anisotropic equations have been derived. This has been performed in the context of Vertical Transverse Isotropy (VTI) where the anisotropy axis is parallel to the vertical direction, and generalized to Tilted Transverse Isotropy (TTI), for which the

anisotropy axis is tilted from the vertical direction. In the more general settings, the tilt angle may vary depending on the space location.

Consider the 2D elastic VTI equations

$$\begin{cases} \partial_t u_x - \frac{1}{\rho}\partial_x \sigma_{xx} - \frac{1}{\rho}\partial_z \sigma_{xz} &= 0 \\ \partial_t u_z - \frac{1}{\rho}\partial_z \sigma_{zz} - \frac{1}{\rho}\partial_x \sigma_{xz} &= 0 \\ \partial_t \sigma_{xx} - c_{11}\partial_x u_x - c_{13}\partial_z u_z &= 0 \\ \partial_t \sigma_{zz} - c_{13}\partial_x u_x - c_{33}\partial_z u_z &= 0 \\ \partial_t \sigma_{xz} - \frac{c_{44}}{2}\left(\partial_x u_z + \partial_z u_x\right) &= 0, \end{cases} \tag{33}$$

where C is the stiffness tensor

$$C = \begin{pmatrix} c_{11} & c_{13} & 0 \\ c_{13} & c_{33} & 0 \\ 0 & 0 & c_{44} \end{pmatrix}. \tag{34}$$

Following the strategy of Duveneck and Bakker [15] , we cancel the S-wave velocity in the equations (33). As we have the relation

$$v_S = \sqrt{c_{44}}, \tag{35}$$

this is equivalent to cancel c_{44} in (33). We obtain the 2D VTI acoustic equations

$$\begin{cases} \partial_t u_x - \frac{1}{\rho}\partial_x \sigma_{xx} &= 0 \\ \partial_t u_z - \frac{1}{\rho}\partial_z \sigma_{zz} &= 0 \\ \partial_t \sigma_{xx} - c_{11}\partial_x u_x - c_{13}\partial_z u_z &= 0 \\ \partial_t \sigma_{zz} - c_{13}\partial_x u_x - c_{33}\partial_z u_z &= 0. \end{cases}$$

These equations can be generalized to the TTI case by introducing the tilt angle $\theta(x)$ (see Duveneck and Bakker [15] for a step by step derivation of the system)

$$\begin{cases} \partial_t u_x - \frac{1}{\rho}\left[\partial_x\left(\cos^2\theta\sigma^\theta_{xx} + \sin^2\theta\sigma^\theta_{zz}\right) + \partial_z\left(\sin\theta\cos\theta\left(\sigma^\theta_{zz} - \sigma^\theta_{xx}\right)\right)\right] = 0 \\ \partial_t u_z - \frac{1}{\rho}\left[\partial_z\left(\sin^2\theta\sigma^\theta_{xx} + \cos^2\theta\sigma^\theta_{zz}\right) + \partial_x\left(\sin\theta\cos\theta\left(\sigma^\theta_{zz} - \sigma^\theta_{xx}\right)\right)\right] = 0 \\ \partial_t \sigma^\theta_{xx} - c_{11}\left[\cos^2\theta\partial_x u_x - \sin\theta\cos\theta(\partial_x u_z + \partial_z u_x) + \sin^2\theta\partial_z u_z\right] \\ \qquad - c_{13}\left[\sin^2\theta\partial_x u_x + \sin\theta\cos\theta(\partial_x u_z + \partial_z u_x) + \cos^2\theta\partial_z u_z\right] = 0 \\ \partial_t \sigma^\theta_{zz} - c_{13}\left[\cos^2\theta\partial_x u_x - \sin\theta\cos\theta(\partial_x u_z + \partial_z u_x) + \sin^2\theta\partial_z u_z\right] \\ \qquad - c_{33}\left[\sin^2\theta\partial_x u_x + \sin\theta\cos\theta(\partial_x u_z + \partial_z u_x) + \cos^2\theta\partial_z u_z\right] = 0. \end{cases} \tag{36}$$

This system can be rewritten in the general first-order hyperbolic form (1) with

$$A_1 = -\begin{pmatrix} 0 & 0 & \frac{1}{\rho}\cos^2\theta & \frac{1}{\rho}\sin^2\theta \\ 0 & 0 & -\frac{1}{\rho}\sin\theta\cos\theta & \frac{1}{\rho}\sin\theta\cos\theta \\ c_{11}\cos^2\theta + c_{13}\sin^2\theta & (c_{13} - c_{11})\sin\theta\cos\theta & 0 & 0 \\ c_{13}\cos^2\theta + c_{33}\sin^2\theta & (c_{33} - c_{13})\sin\theta\cos\theta & 0 & 0 \end{pmatrix} \tag{37}$$

$$A_2 = -\begin{pmatrix} 0 & 0 & -\frac{1}{\rho}\sin\theta\cos\theta & \frac{1}{\rho}\sin\theta\cos\theta \\ 0 & 0 & \frac{1}{\rho}\sin^2\theta & \frac{1}{\rho}\cos^2\theta \\ (c_{13} - c_{11})\sin\theta\cos\theta & c_{11}\sin^2\theta + c_{13}\cos^2\theta & 0 & 0 \\ (c_{33} - c_{13})\sin\theta\cos\theta & c_{13}\sin^2\theta + c_{33}\cos^2\theta & 0 & 0 \end{pmatrix} \tag{38}$$

and the zero-order term

$$A_0(x) = \begin{pmatrix} 0 & 0 & \frac{1}{\rho}\partial_x\left(\cos^2\theta\right) - \frac{1}{\rho}\partial_z\left(\sin\theta\cos\theta\right) & \frac{1}{\rho}\partial_x\left(\sin^2\theta\right) + \frac{1}{\rho}\partial_z\left(\sin\theta\cos\theta\right) \\ 0 & 0 & \frac{1}{\rho}\partial_z\left(\sin^2\theta\right) - \frac{1}{\rho}\partial_x\left(\sin\theta\cos\theta\right) & \frac{1}{\rho}\partial_z\left(\cos^2\theta\right) + \frac{1}{\rho}\partial_x\left(\sin\theta\cos\theta\right) \\ 0 & 0 & 0 & 0 \\ 0 & 0 & 0 & 0 \end{pmatrix}. \tag{39}$$

The matrices A_1 and A_2 have four distinct eigenvalues denoted by

$$\lambda^+_{jP}, \quad \lambda^-_{jP}, \quad \lambda^+_{jS}, \quad \lambda^-_{jS}, \quad j = 1, 2. \tag{40}$$

We can explicitly compute these eigenvalues. We use the definition of the Thomsen parameters for anisotropy (Thomsen [37]) which relates the stiffness tensor coefficient and the density to the vertical P-wave velocity v_P and dimensionless parameters ϵ and δ. In the particular case of TI acoustic approximation, we have

$$\left\{ \begin{array}{rcl} c_{11} & = & \rho v_P^2 (1+2\epsilon), \\ c_{33} & = & \rho v_P^2, \\ c_{13} & = & \rho v_P^2 \sqrt{1+2\delta} \end{array} \right. \tag{41}$$

The eigenvalues of A_1 and A_2 are given by

$$\lambda_{1P}^{\pm} = \pm v_P \sqrt{\frac{a_1 + \sqrt{\Delta_1}}{2}}, \quad \lambda_{1S}^{\pm} = \pm v_P \sqrt{\frac{a_1 - \sqrt{\Delta_1}}{2}},$$

$$a_1 = 1 + 2\epsilon \cos^2\theta, \quad \Delta_1 = \Big((1+2\epsilon)\cos^2\theta + \sin^2\theta\Big)^2 + 8(\epsilon - \delta)\cos^2\theta \sin^2\theta.$$

$$\lambda_{2P}^{\pm} = \pm v_P \sqrt{\frac{a_2 + \sqrt{\Delta_2}}{2}}, \quad \lambda_{2S}^{\pm} = \pm v_P \sqrt{\frac{a_2 - \sqrt{\Delta_2}}{2}},$$

$$a_2 = 1 + 2\epsilon \sin^2\theta, \quad \Delta_2 = \Big((1+2\epsilon)\sin^2\theta + \cos^2\theta\Big)^2 + 8(\epsilon - \delta)\cos^2\theta \sin^2\theta.$$

Note that the norm of the 4 eigenvalues $\lambda_{jS}^{\pm}$ is lower than the norm of the eigenvalues $\lambda_{jP}^{\pm}$. The eigenvalues $\lambda_{jS}^{\pm}$ are actually associated with residual S modes, remaining even after the S-wave velocity is forced to 0 along the anisotropy axis. This is related to a well known result on acoustic TI models: the S-wave velocity is zero only in the direction aligned with the anisotropy symmetry axis, and in the direction normal to this axis (Grechka et al. [17]). In other directions, S-waves can propagate if excited.

The selective damping strategy associated with the SMART layer method can thus be used here to damp spurious S-waves directly into the domain of interest, around the source and interfaces where high amplitude reflections generate also spurious S-waves. We define the projectors $P_{jS}^{\pm}$ on the eigenspaces

$$\ker\Big(A_j - \lambda_{jS}^{\pm} I_4\Big). \tag{42}$$

The S-wave filter consists in introducing the zero-order term $B_{loc}(x)$ into (1) such that

$$B_{loc}(x) = loc(x)\Big(P_{1S}^{+} + P_{1S}^{-} + P_{2S}^{+} + P_{2S}^{-}\Big),$$

where $loc(x)$ is a damping coefficient which is zero everywhere except in the region where we wish to damp the S-waves.

5. Numerical experiments

5.1. Settings

We perform the numerical experiments on the 2D acoustic TI system (36). We use the rotated staggered-grid finite difference scheme of Saenger et al. [35] which is adapted to these equations. We implement a fourth-order in space and second-order in time discretization.

The choice of the damping coefficient is made according to the study of Hu [21] such that

$$d_j^{-}(x_j) = \frac{8(n+1)}{L_j}\left(\frac{a_j - x_j}{L_j}\right)^n, \quad d_j^{+}(x_j) = \frac{8(n+1)}{L_j}\left(\frac{x_j - b_j}{L_j}\right)^n, \tag{43}$$

where $n \in \mathbb{N}$. In the numerical experiments we choose third order polynomials and set n to 3. In all experiments, a free surface condition is implemented on top of the model. Homogeneous Dirichlet boundary conditions are used at the external boundaries of the left, right and bottom layers.

We use an explosive Ricker source located at x_S, of the form

$$s(x,t) = \delta(x - x_S)\varphi(t), \tag{44}$$

where $\delta(x)$ is the Dirac delta function in space, and

$$\varphi(t) = \Big[1 - 2\omega^2(t-t_0)^2\Big]e^{-\omega^2(t-t_0)^2}, \quad \omega = \Pi f. \tag{45}$$

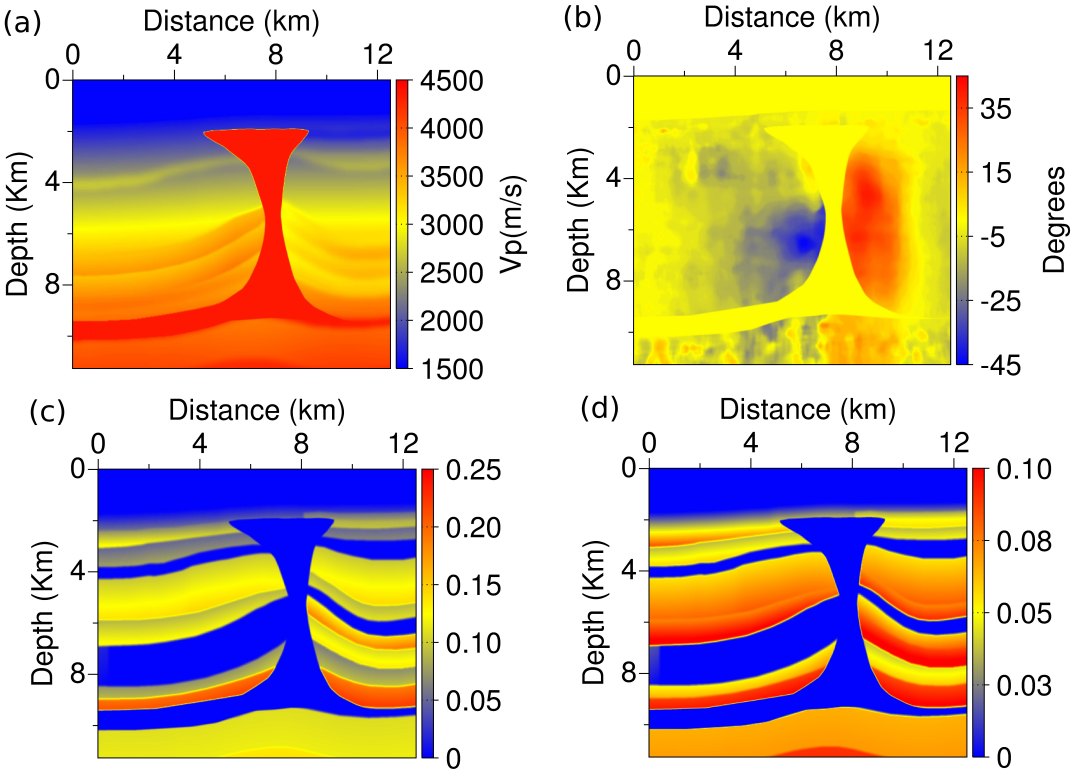

Figure 1: (a) vertical P-wave velocity, (b) tilt angle, (c) Thomsen parameter ϵ, (d) Thomsen parameter δ.

In the formula (45), f is the central frequency of the Ricker. In the following experiments, f is set to 15 Hz. We apply the weights w_x and w_z to the normal-stress components of the explosive source such that shear strain is minimized at the source. Under the general formulation (1), the source term we use is thus

$$s(x,t) = \begin{bmatrix} 0 & 0 & w_x s & w_z s \end{bmatrix}^T. \tag{46}$$

Following the strategy proposed by Operto et al. [33] the weights $(w_x, w_z) \in \mathbb{R}^2$ are defined by

$$\begin{cases} w_x = \dfrac{1 + 2\epsilon + \sqrt{1+2\delta}}{1 + \epsilon + \sqrt{1+2\delta}} \\ w_z = \dfrac{1 + \sqrt{1+2\delta}}{1 + \epsilon + \sqrt{1+2\delta}}. \end{cases} \tag{47}$$

5.2. Stability test on the BP 2007 benchmark model

In 2007, BP released a public benchmark model representative of the geology of the Gulf of Mexico. This model contains a vertical P-wave velocity model as well as Thomsen parameters ϵ and δ and a tilt angle map. We focus on a part of this model located around the middle salt dome. The resulting P-wave velocity, ϵ, δ and tilt angle models are presented in Figure 1.

We locate the source close to the top of the model such that $x_1 = 7$ km, $x_2 = 0.05$ km. The spatial discretization step is set to 25 m both in horizontal and vertical directions. We ensure at least 4 discretization point by shortest wavelength, according to our choice of a 4th order finite-difference scheme. The time discretization step is selected so as to satisfy the CFL condition (Martin and Komatitsch [26]).

$$\Delta t \leq \frac{1}{\sqrt{2}\|v_P\|_\infty \sqrt{\frac{1}{\Delta x^2} + \frac{1}{\Delta z^2}}} \tag{48}$$

The simulation time is set to 12 s. We first compute a reference solution in a domain large enough to ensure no reflection at the boundary. We then compute solutions using PML and SMART layers. We compare

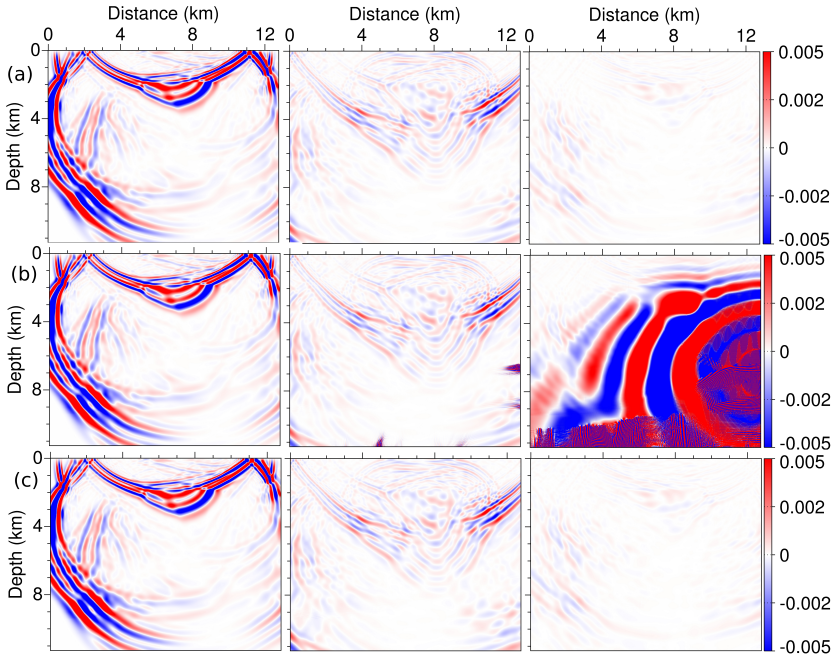

Figure 2: Pressure wavefield snapshots in the domain of interest at time $t = 4.2$ s, 7.8 s and 12 s (from left to right). Reference wavefield (row a). PML wavefield (row b), SMART wavefield (row c). The PML amplification starts at time $t = 7.8$ s on the right and bottom edges of the domain and contaminates almost all the domain at final time $t = 12$ s

snapshots of the PML and SMART wavefields with the reference wavefields in Figure 2. As can be seen, the PML solution suffers from an exponentially growing mode which contaminates the whole domain of interest at the end of the computation. In comparison, the SMART layer solution remains stable (no growing modes appear) as expected from the stability analysis of Section 2. The SMART layer wavefield shows a satisfactory agreement with the reference solution. This experiment emphasizes the robustness of the SMART layer in a strongly heterogeneous and anisotropic model, compared to the PML approach.

5.3. Accuracy comparison between PML, SPONGE, and SMART layers

We perform an accuracy comparison between the three different layer methods PML, SPONGE and SMART. The SPONGE layer method of Cerjan et al. [12] amounts to add to the initial hyperbolic system (1) a zero-order term of the form

$$B(x)u = \sum_{i=1}^{d} \left(d_j^+(x_j) + d_j^-(x_j) \right) u \tag{49}$$

Compared to (9), this amounts to choose the identity matrix instead of the projectors on the eigenspaces of the matrices A_j. This simple choice yields a dissipative layer: this can be shown easily following the proof we give in Section 2.2. However, the SPONGE strategy is known to be poorly accurate, especially for waves arriving at grazing angles. We investigate here if the SMART layer method is a more accurate alternative to the SPONGE layer, with the warranty of a dissipative behavior.

We set a simple synthetic example in a homogeneous model with the following characteristics

- $v_P = 2000$ m.s^{-1}, $\rho = 1000$ kg.m^{-3},
- $\epsilon = \delta = 0.3$
- $\theta = 36^\circ$

We set on purpose elliptical anisotropy (the value of ϵ is equal to the value of δ). In this particular case, the 2D acoustic TI equation reduce to a simpler system for which the PML are stable. We thus can compare the accuracy of the three layer strategies in terms of reflectivity at the interface between the domain of interest and the layer. The domain of interest is a square of 2 km by 2 km. The recording time is set to 3 s. The

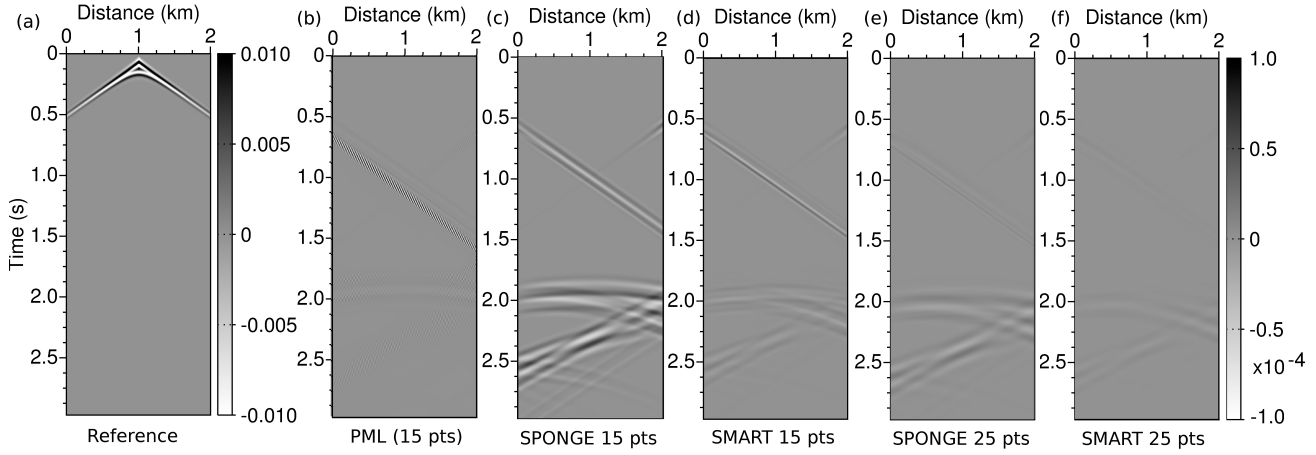

Figure 3: Reference seismogram (a). Residuals seismogram with PML 15 grid points width (b), SPONGE with 15 grid points, SMART with 15 grid points (c), SPONGE with 25 grid points (d), SMART with 25 grid points (e). The scale of the residual is 2 orders of magnitude lower than for the reference wavefields.

spatial discretization step is set to 10 m to ensure 4 points by wavelength. The time discretization step is set so that it satisfies the CFL condition (48). We implement a free surface condition on top. We compute a reference seismogram for a source located at $x_1 = 1$ km, $z_2 = 0.05$ km and an array of receivers located all along the free surface at the same depth as the source. This reference solution is computed in a domain large enough to ensure no reflection at the boundaries during the recording time. It is presented in Figure 3, along with residual seismograms obtained from the difference between the reference seismogram and the seismograms obtained using the different layer methods, with different thickness.

We observe from Figure 3 the excellent accuracy of the PML solution in this case. The color-scale for the residual seismogram is two orders of magnitude lower than the color-scale used for the reference seismogram, and the residual energy in the PML seismogram is weak. Using the same layer thickness (15 discretization points), the SPONGE layer method yields significantly more energetic residuals. In comparison, the SMART layer appears to be less reflective than the SPONGE layer: the amplitude of the spurious reflections generated by the SMART layer is weaker. When the layer thickness is increased to 25 discretization points, the SPONGE layer still produces non negligible spurious reflections, while the SMART layer almost reaches the accuracy of the PML layer with 15 discretization points.

From this comparison, we see that the SMART layer is not as accurate as the PML method. This is expected, as the SMART method is not perfectly matched: the reflection coefficient at the interface between the domain of interest and the layer is zero only for waves arriving at normal incidence. On the other hand, the SMART layer method represents a significant improvement with respect to the SPONGE layer in terms of accuracy, as the amplitude of spurious reflection seems to be significantly reduced. We thus conclude that the SMART layer strategy is a better choice than PML or SPONGE layers when PML amplification problem arises, due to numerical schemes or the presence of anisotropy.

5.4. SMART layers as a S-waves filter for acoustic TI modeling

We take the same settings as for the previous experiment excepted that we now choose an anelliptical anisotropy. We set ϵ and δ to $\epsilon = 0.3$ and $\delta = 0.1$. We also locate a planar reflector at the depth $z = 0.5$ km along the x axis. This reflector is associated with a density discontinuity. In this configuration, we observe the propagation of spurious S-waves generated at the source and at the reflector locations. Due to P-S conversion, reflector behaves as a secondary S-waves source, after the main wavefront has been reflected. We investigate if the SMART strategy can be used as an efficient S-waves filter. To this purpose, we test two different localization patterns. The first one has a Gaussian shape centered on the source. The second one uses the same Gaussian pattern around the source and an additional ellipsoidal pattern around the reflector. The results are presented in Figure 4.

We observe in Figure 4 that when no filter is used, (Fig 4(a), 4(d)), the source generates non negligible spurious S-waves. When the wavefield reflects on the planar interface, additional S-waves are also gener-

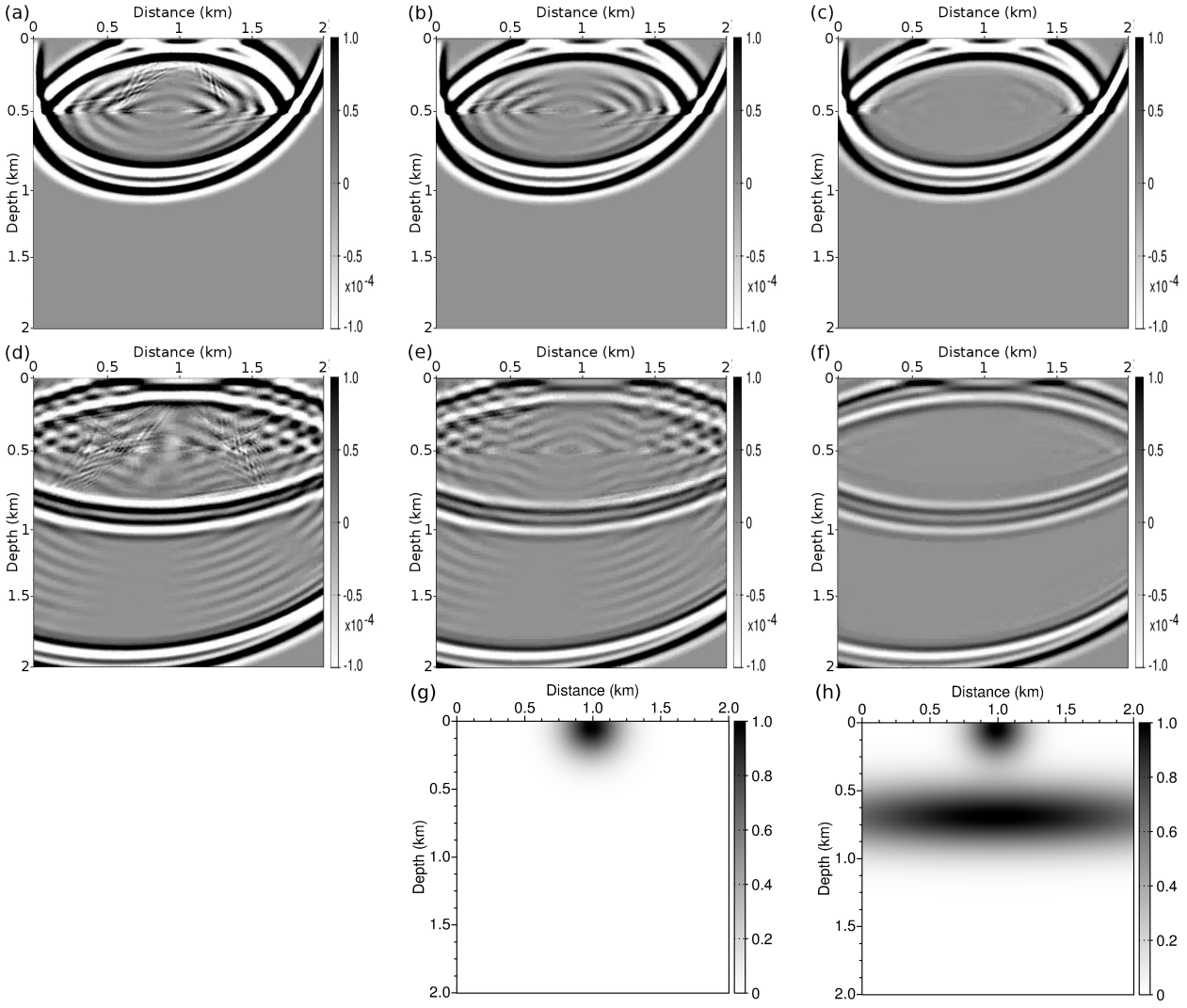

Figure 4: Snapshots of the wavefield at $t = 1.6$ s, using no filter (a), using a filter around the source (b), using a filter around the source and the reflector (c). Snapshots of the wavefield at $t = 3$ s, using no filter (d), using a filter around the source (e), using a filter around the source and the reflector (f). Shape of the filter around the source (g), around the source and the reflector (h).

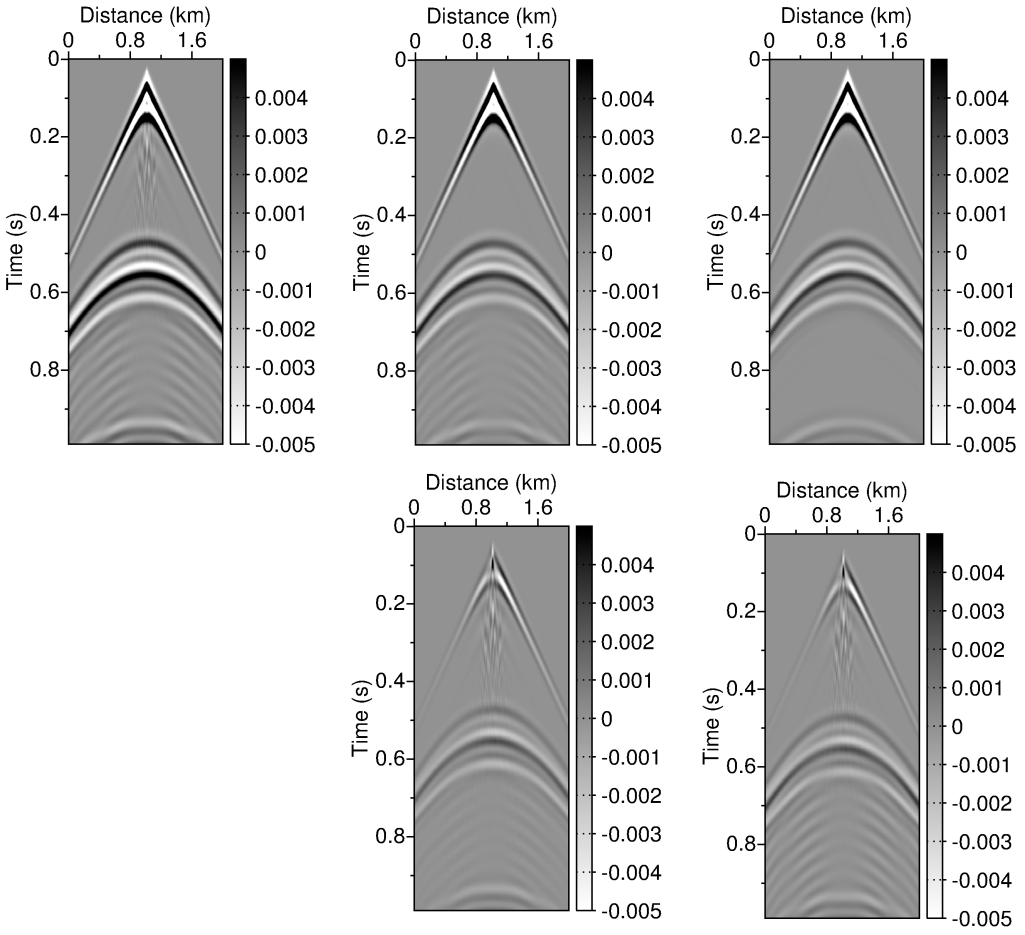

Figure 5: Seismograms obtained with a surface acquisition system. No filter (a), filter around the source (b), filter around the source and the reflector (c). Differential seismogram between (a) no filter and (b) filter around the source (d). Differential seismogram between (a) no filter and (c) filter around the source and the reflector (e).

ated. The strategy consisting in damping the S-waves uniquely at the source may not be appropriated in this case. In Figures 4(b), 4e), we see that even if S-waves have been removed from the source impulse signal, the reflector still behaves as a secondary S-wave source. In contrast, when S-waves are damped simultaneously at the source and around the reflector, the wavefield which remains in the domain of interest seems to be constituted almost exclusively of P-waves. Note that, however, the amplitude of the main P-wavefront is decreased with respect to the case where no filtering strategy is applied. This phenomenon is emphasized on the seismograms presented in Figure 5. We use a surface acquisition system with a source located near the surface and centered with respect to the horizontal axis. The recording time is set to 1 s. The separation in the damping between S- and P-waves is not exact in the numerical approximation, as it relies on high frequency assumptions. In practice, we are not in the high frequency regime, therefore, P-waves are also impacted when they travel through the filtering zones. This prevent from defining an S-wave filter in the whole domain of interest. For application to real case study, it would be necessary to design the filter on local properties of the medium such that it will be the most narrow possible for not altering strongly P-wave amplitude. This delineation could be performed through spatial gradient analysis (identification of the jump location in the material properties), or using more sophisticated edge detection techniques based on wavelet transform, as for instance proposed in Operto et al. [32].

6. Conclusion

Depending on the discretization method which is used, or when anisotropy is accounted for, the state-of-the-art absorbing boundary condition method for elastodynamics equations, namely the PML approach

(Bérenger [8]), can become amplifying and yield unmanageable instabilities, especially when considering inversion workflow. This study has shown that the SMART layer method introduced by Halpern et al. [18] is a interesting alternative to PML for elastodynamics equations, especially when considering anisotropic propagation.

We show that the SMART layer method is unconditionally dissipative for symmetrizable first-order hyperbolic system, and we recall that the elastodynamics equations satisfy this assumption, building explicitly a symmetrizer for these equations, based on the compliance matrix. Numerical experiments emphasize the robustness of the SMART layer. In a strongly heterogeneous and anisotropic environment, the SMART layer method remains stable, while the PML exhibits an amplifying behavior. The SMART layer is not perfectly matched, therefore less accurate than PML method in terms of reflectivity at the interface between the domain of interest and the layer. However, we show that the accuracy of the PML can be reached by the SMART layer at the expense of a reasonable increase of the layer size. The accuracy of the SMART layer is also compared to another class of dissipative layer, known as SPONGE layers, introduced by Cerjan et al. [12]. Our numerical results indicate that the SMART layer outperforms SPONGE layers in terms of accuracy. Hence, when stability is mandatory, SMART layers method appears as the method of choice for elastodynamics.

We also explore another feature of the SMART layer strategy, related to the selective damping of the different components of the solution at the basis of the method. In the particular case of acoustic anisotropic models, spurious S-waves can be damped directly at the locations where they are generated, namely at the source and around strong interfaces of the subsurface model. Numerical experiments in a homogeneous medium show satisfactory results for such an application. This could be an alternative to pure pseudo P-wave modeling techniques such as the one promoted by Xu and Zhou [39]

From this study, some perspectives of future work can be drawn. The first one is related to the implementation of the SMART method in the context of 3D fully anisotropic elastodynamics equations using a Lebedev scheme. Investigation will also be performed for the extension of the SMART method to second-order hyperbolic systems. Finally, the method should be used in the context of seismic imaging method such as FWI or RTM.

Acknowledgements

This study was partially funded by the SEISCOPE II consortium (*http://seiscope2.osug.fr*), sponsored by BP, CGG, CHEVRON, EXXON-MOBIL, JGI, PETROBRAS, SAUDI ARAMCO, SHELL, SINOPEC, STATOIL, TOTAL and WESTERNGECO. This study was granted access to the HPC facilities of CIMENT (Université Joseph Fourier, Grenoble). Many thanks are due to Laurence Halpern and Jeffrey Rauch for their advice and inspiring comments.

[1] Abarbanel, S., Gottlied, D., and Hesthaven, J. S. (1999). Well-posed perfectly matched layers for advective acoustics. *Journal of Computational Physics*, 154(2):266–283.

[2] Alkhalifah, T. (1998). Acoustic approximations for processing in transversely isotropic media. *Geophysics*, 63:623–631.

[3] Alkhalifah, T. (2000). An acoustic wave equation for anisotropic media. *Geophysics*, 65:1239–1250.

[4] Appelö, D. and Kreiss, G. (2006). A new absorbing layer for elastic waves. *Journal of Computational Physics*, 215(2):642 – 660.

[5] Basu, U. and Chopra, A. K. (2003). Perfectly matched layers for time-harmonic elastodynamics of unbounded domains: theory and finite-element implementation. *Computer Methods in Applied Mechanics Engineering*, 192:1337–375.

[6] Baysal, E., Kosloff, D., and Sherwood, J. (1983). Reverse time migration. *Geophysics*, 48:1514–1524.

[7] Becache, E., Fauqueux, S., and Joly, P. (2003). Stability of Perfectly Matched Layers, Group Velocities and Anisotropic Waves. *Journal of Computational Physics*, 188:399–433.

[8] Bérenger, J.-P. (1994). A perfectly matched layer for absorption of electromagnetic waves. *Journal of Computational Physics*, 114:185–200.

[9] Bérenger, J. P. (1996). Three-dimensional perfectly matched layer for the absorption of electromagnetic waves. *Journal of Computational Physics*, 127(2):363–379.

[10] Bermúdez, A., Hervella-Nieto, L., Prieto, A., and Rodríguez, R. (2007). An optimal perfectly matched layer with unbounded absorbing function for time-harmonic acoustic scattering problems. *Journal of Computational Physics*, 223(2):469–488.

[11] Burridge, R. (1996). Elastic waves in anisotopric media. Schlumberger-Doll Research.

[12] Cerjan, C., Kosloff, D., Kosloff, R., and Reshef, M. (1985). A nonreflecting boundary condition for discrete acoustic and elastic wave equations. *Geophysics*, 50(4):2117–2131.

[13] Collino, F. and Tsogka, C. (2001). Application of the perfectly matched absorbing layer model to the linear elastodynamic problem in anisotropic heterogeneous media. *Geophysics*, 66:294–307.

[14] Diaz, J. and Joly, P. (2006). A time domain analysis of pml models in acoustics. *Computer Methods in Applied Mechanics and Engineering*, 195(29-32):3820–3853.

[15] Duveneck, E. and Bakker, P. M. (2011). Stable P-wave modeling for reverse-time migration in tilted TI media. *Geophysics*, 76(2):S65–S75.

[16] Etienne, V., Chaljub, E., Virieux, J., and Glinsky, N. (2010). An hp-adaptive discontinuous Galerkin finite-element method for 3D elastic wave modelling. *Geophysical Journal International*, 183(2):941–962.
[17] Grechka, V., Zhang, L., and Rector III, J. W. (2004). Shear waves in acoustic anisotropic media. *Geophysics*, 69:576–582.
[18] Halpern, L., Petit-Bergez, S., and Rauch, J. (2011). The Analysis of Matched Layers. *Confluentes Mathematici*, 3(2):159–236.
[19] Hastings, F. D., Schneider, J. B., and Broschat, S. L. (1996). Application of the perfectly matched layer (PML) absorbing boundary condition to elastic wave propagation. *Journal of Acoustical Society of America*, 100:3061–3069.
[20] Hesthaven, J. (1998). On the analysis and construction of perfectly matched layers for the linearized euler equations. *Journal of Computational Physics*, 142:129–147.
[21] Hu, F. Q. (1996). On absorbing boundary conditions for linearized euler equations by a perfectly matched layer. *Journal of Computational Physics*, 129(1):201–219.
[22] Israeli, M. and Orszag, S. A. (1981). Approximation of radiation boundary conditions. *Journal of Computational Physics*, 41:115–135.
[23] Komatitsch, D. and Martin, R. (2007). An unsplit convolutional perfectly matched layer improved at grazing incidence for the seismic wave equation. *Geophysics*, 72(5):SM155–SM167.
[24] Komatitsch, D. and Tromp, J. (2003). A Perfectly Matched Layer absorbing boundary condition for the second-order seismic wave equation. *Geophysical Journal International*, 154(1):146–153.
[25] Kreiss, H. O. and Lorenz, J. (2004). *Initial-boundary value problems and the Navier-Stokes equations*. Classics in Applied Mathematics 47, SIAM.
[26] Martin, R. and Komatitsch, D. (2009). An unsplit convolutional perfectly matched layer technique improved at grazing incidence for the viscoelastic wave equation. *Geophysical Journal International*, 179:333–344.
[27] Martin, R., Komatitsch, D., and Ezziani, A. (2008). An unsplit convolutional perfectly matched layer improved at grazing incidence for seismic wave propagation in poroelastic media. *Geophysics*, 73(4):51–61.
[28] Métivier, L., Bretaudeau, F., Brossier, R., Operto, S., and Virieux, J. (2014a). Full waveform inversion and the truncated Newton method: quantitative imaging of complex subsurface structures. *Geophysical Prospecting*, 62:1353–1375.
[29] Métivier, L., Brossier, R., Labbé, S., Operto, S., and Virieux, J. (2014b). A robust absorbing layer for anisotropic seismic wave modeling. *Journal of Computational Physics*, 279:218–240.
[30] Métivier, L., Brossier, R., Virieux, J., and Operto, S. (2013). Full Waveform Inversion and the truncated Newton method. *SIAM Journal On Scientific Computing*, 35(2):B401–B437.
[31] Meza-Fajardo, K. C. and Papageorgiou, A. S. (2008). A nonconvolutional, split-field, perfectly matched layer for wave propagation in isotropic and anisotropic elastic media: Stability analysis. *Bulletin of the Seismological Society of America*, 98(4):1811–1836.
[32] Operto, S., Virieux, J., Hustedt, B., and Malfanti, F. (2002). Adaptive wavelet-based finite-difference modelling of SH-wave propagation. *Geophysical Journal International*, 148(3):477–499.
[33] Operto, S., Virieux, J., Ribodetti, A., and Anderson, J. E. (2009). Finite-difference frequency-domain modeling of visco-acoustic wave propagation in two-dimensional TTI media. *Geophysics*, 74 (5):T75–T95.
[34] Qi, Q. and Geers, T. L. (1998). Evaluation of the perfectly matched layer for computational acoustics. *Journal of Computational Physics*, 139(1):166–183.
[35] Saenger, E. H., Gold, N., and Shapiro, S. A. (2000). Modeling the propagation of elastic waves using a modified finite-difference grid. *Wave motion*, 31:77–92.
[36] Tago, J., Métivier, L., and Virieux, J. (2014). SMART layers: a simple and robust alternative to PML approaches for elastodynamics. *Geophysical Journal International*, 199(2):700–706.
[37] Thomsen, L. A. (1986). Weak elastic anisotropy. *Geophysics*, 51:1954–1966.
[38] Virieux, J. and Operto, S. (2009). An overview of full waveform inversion in exploration geophysics. *Geophysics*, 74(6):WCC1–WCC26.
[39] Xu, S. and Zhou, H. (2014). Pure quasi- P wave calculation in anisotropic media. In *SEG Technical Program Expanded Abstracts 2014*, pages 3887–3891.